CrossMark

Coupled Crystal Plasticity–Phase Field Fracture Simulation Study on Damage Evolution Around a Void: Pore Shape Versus Crystallographic Orientation

MARTIN DIEHL [ID],[1,3] MARCEL WICKE,[2] PRATHEEK SHANTHRAJ,[1] FRANZ ROTERS,[1] ANGELIKA BRUECKNER-FOIT,[2] and DIERK RAABE[1]

1.—Max-Planck-Institut für Eisenforschung GmbH, Max-Planck-Straße 1, 40237 Düsseldorf, Germany. 2.— Institute for Materials Engineering, University of Kassel, Moenchebergstraße 3, 34109 Kassel, Germany. 3.—e-mail: m.diehl@mpie.de

Various mechanisms such as anisotropic plastic flow, damage nucleation, and crack propagation govern the overall mechanical response of structural materials. Understanding how these mechanisms interact, i.e. if they amplify mutually or compete with each other, is an essential prerequisite for the design of improved alloys. This study shows—by using the free and open source software DAMASK (the Düsseldorf Advanced Material Simulation Kit)—how the coupling of crystal plasticity and phase field fracture methods can increase the understanding of the complex interplay between crystallographic orientation and the geometry of a void. To this end, crack initiation and propagation around an experimentally obtained pore with complex shape is investigated and compared to the situation of a simplified spherical void. Three different crystallographic orientations of the aluminum matrix hosting the defects are considered. It is shown that crack initiation and propagation depend in a non-trivial way on crystallographic orientation and its associated plastic behavior as well as on the shape of the pore.

INTRODUCTION

The mechanical performance of metallic materials depends on various coupled—partly competing and partly enhancing—mechanisms. Understanding these mechanisms and their nonlinear coupling is an essential prerequisite for the design of new damage-tolerant alloys. Hence, various numerical modeling strategies have been developed to investigate the influence of different mechanisms on the mechanical response of structural materials. On the one hand, crystal plasticity simulation techniques[1] can predict mechanical behavior of polycrystalline materials based on the interplay between phases, grains, and subgrains in dependence of the anisotropic elastic and plastic behavior of these features. On the other hand, damage and fracture modeling[2] enables insights into stress and strain re-partitioning due to local material softening. Combining both approaches hence enables investigation of the local stress and strain evolution based on concurrent evolution of plastic deformation, crystallographic re-orientation and damage-induced softening.[3–5] In this study, such an approach for coupling a crystal plasticity formulation with a phase field fracture model[6–10] is used to study the mechanical behavior of experimentally obtained microstructures. The approach presented here is implemented in the free Düsseldorf Advanced Material Simulation Kit (DAMASK)[15] which is available as free and open source software.

The work is motivated by experimental investigations that show the detrimental effect of porosity on the fatigue life of commercial Al-Si cast alloys.[11,12] Recent improvements in x-ray computer tomography techniques allow the characterization of such defects in these alloys with high spatial resolution. We focus on a single pore obtained by x-ray computer tomography (also termed micro-computed tomography, μ-CT) and simulate fracture evolution around this pore embedded in a single crystal material.* Simulation studies investigating the stress concentration around pores acquired by

---

*The single crystal assumption is motivated by experimental investigations revealing that transcrystalline crack propagation dominates in the material at hand.

μ-CT have been recently published assuming either linear elastic material behavior[13] or isotropic plasticity.[14] Here, we go beyond such approaches and model the elastic and plastic anisotropy of fcc crystals as well as damage-induced softening. However, since fatigue simulations at the microstructural level are computationally not feasible without allowing for certain constitutive simplifications, quasi-static loading conditions are applied here in order to understand the dependence of damage evolution on both the crystallographic orientation of the adjacent aluminum matrix and the shape of the pore. The μ-CT mapping method which was used to observe the pore does not allow for the concurrent determination of the crystallographic orientation of the surrounding matrix. Therefore, three different crystallographic orientations have been assigned to the matrix material for conducting a pertinent parameter study on the influence of host orientation on crack initiation and growth. Additionally, to investigate the effect of the pore geometry, a second simulation series has been conducted for which the complex-shaped pore as obtained by μ-CT is replaced by a spherical void with approximately the same volume.

The study is structured as follows: first the modeling approach, namely the crystal plasticity and the phase field fracture model as well as the numerical solution strategy as implemented into DAMASK are presented. Then, the simulation details, including details and specific features associated with the experimental characterization technique, are given. After presenting and discussing the results, we render an outlook on possible further improvements of the employed approach.

MODELING STRATEGY

The multiphysics simulation package DAMASK[15] provides both the crystal plasticity and the phase field fracture model in a coupled way.[9] A hybrid finite element-spectral solver, which allows an easy and direct use and mapping of the experimentally obtained microstructure data, is employed to solve the mechanical boundary value problem and the governing phase field kinetic evolution predicting the onset and growth of damage. Details of these three modeling ingredients are presented in the following.

Crystal Plasticity

A conventional viscoplastic phenomenological model for crystal plasticity[16,17] is used to describe the behavior of the aluminum fcc crystal. The model is based on the assumption that plastic slip γ occurs on a slip system α when the resolved shear stress τ^α exceeds a critical value ξ^α. The critical shear stress on each of the 12 fcc slip systems is assumed to evolve from an initial value, ξ_0 to a saturation value ξ_∞ due to slip on all $\langle 011 \rangle \{111\}$ systems $\beta = 1, \ldots, 12$

according to the relationship $\dot{\xi}^\alpha = h_0 \, |\dot{\gamma}^\beta| \, |1 - \xi^\beta / \xi_\infty^\beta|^a \mathrm{sgn}(1 - \xi^\beta / \xi_\infty^\beta) \, h_{\alpha\beta}$ with initial hardening h_0, interaction coefficients $h_{\alpha\beta}$, and a numerical parameter a. The shear rate on system α is then computed as $\dot{\gamma}^\alpha = \dot{\gamma}_0 |\tau^\alpha / \xi^\alpha|^n \mathrm{sgn}(\tau^\alpha / \xi^\alpha)$ with the inverse shear rate sensitivity n and reference shear rate $\dot{\gamma}_0$. The sum of the shear rates on all systems determines the plastic velocity gradient for the finite strain formulation used in DAMASK.[15]

Phase Field Modeling of Fracture

The phase field method for fracture[6–8] is employed, where a scalar non-local damage variable, φ, is introduced to track the transition between the initially undamaged ($\varphi = 1$) and fully damaged regions ($\varphi = 0$). The method is based on the variational theory of brittle fracture,[18] but is closely related to gradient models for brittle[19,20] and ductile[21] damage. In the current work, a brittle damage model is used, which is driven by the release of stored elastic energy at a material point, i.e. $\psi_E = \frac{1}{2}\varphi^2 \mathbf{S} \cdot \mathbf{E}$, where there is a continuous release of the stored elastic strain energy density ($\mathbf{S}$: 2nd Piola-Kirchhoff stress, $\mathbf{E}$: elastic Green-Lagrange strain), ψ_E, from an undamaged state to a fully damaged state. Resisting the creation of a crack surface is the associated surface tension, which takes the following form in a phase field setting:

$$\psi_{\mathrm{surf}} = \frac{1}{2} g_0 l_0 |\nabla\varphi|^2 + \frac{g_0}{l_0}(1 - \varphi), \qquad (1)$$

with fracture surface energy g_0 and characteristic length scale l_0.

Classical Ginzburg–Landau relaxation of the total energy results in the following boundary value problem associated with the evolution of φ

$$\dot{\varphi} = -M\left[2\varphi\,\mathbf{S}\cdot\mathbf{E} - \frac{g_0}{l_0} - \nabla g_0 l_0 \nabla\varphi\right], \qquad (2)$$

with mobility M.

Details about the phase field model and its coupling with crystal plasticity are described elsewhere.[9,10]

Numerical Solver

The simulations are conducted using a hybrid finite element–spectral[22,23] discretization coupled to DAMASK. Usage of the spectral method approach based on the fast Fourier transform was pioneered by Moulinec and Suquet[24] and has gained significant attention in computational material mechanics.[25,26] Besides the computational performance—especially when simulating periodic microstructures—one significant advantage of the spectral method is the straightforward use of experimental datasets consisting of regularly arranged measurement points. One drawback of the early spectral

method variants, namely the poor convergence rate for materials with a high difference in stiffness or strength, has been overcome by the use of sophisticated root-finding algorithms instead of the original fix-point scheme.[23,27,28] The collocation-based discretization approach typically used for spectral solvers leads to oscillations in the vicinity of strain or stress jumps that are caused by Gibbs phenomenon. Since these oscillations might introduce significant numerical artifacts in the case of brittle damage modeling and a finite element-based spectral discretization[29,30] is not available within DAMASK, a hybrid finite element–spectral approach is used for the presented study.

SIMULATION SETUP

Geometry Definition

The hexahedral volume elements used in this study have an edge length of $250\,\mu m$ and are discretized into $100 \times 100 \times 100$ points of which 2.7% pertain to the void. To investigate the influence of crystallographic orientation, three different orientations are assigned to the matrix material: cube, rotated cube, and P. In Bunge Euler notation $(\varphi_1,\ \Phi,\ \varphi_2)$ these orientations read in degree (0.0, 0.0, 0.0), (45.0, 0.0, 0.0), and (54.7, 45.0, 0.0).

Realistic Pore The shape of the investigated pore is obtained using a Zeiss Xradia 520 Versa x-ray μ-CT. With a resolution of up to $1\,\mu m$, this μ-CT enables an accurate reconstruction of internal defects in the investigated Fe-rich Al-Si-Cu alloy based on a frontal scanning of the rotating sample. Details on material processing, chemical composition, and experimental procedure are published elsewhere.[13] After reconstruction of the initial microstructure (Fig. 1a), the following post-processing steps have been applied using the Python package scikit-image:[31] (1) denoising using a non-local means filter, Fig. 1b; (2) placing markers based on a threshold, Fig. 1c; (3) segmenting with a random walker algorithm,[32] Fig. 1d; and (4) removing all features consisting of less than 5000 voxel.

Finally, a $100 \times 100 \times 100$ voxel subvolume containing one complex-shaped pore comprised out of 26,969 points (Fig. 2a) was extracted for the following simulations using a realistic pore shape. The complex shape of the pore, with many ramified branches consisting of alternating convex and concave regions, is representative for shrinkage pores found in the investigated material class.[13,14] As a measure inspired by the surface-to-volume ratio that allows quantifying the complexity of a given shape, we calculated the ratio of total voxels in the pore to voxels located at the surface of the pore as 0.675.

Idealized Pore To investigate the influence of the pore geometry, a second volume element containing a pore with idealized shape is created. To this end, a spherical inclusion with diameter of 37 points (26,745 points in the volume) is placed in the center
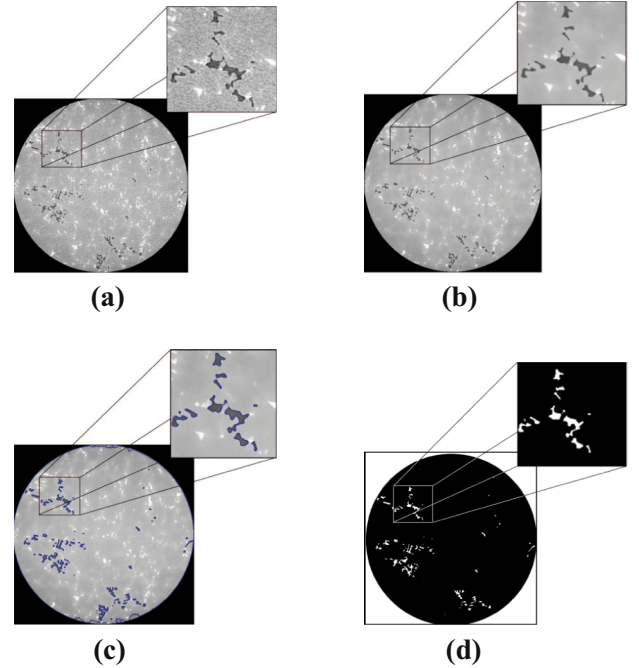

Fig. 1. Top view on the experimentally obtained data at different post-processing states. (a) Imported. (b) Filtered. (c) Marked. (d) Segmented. Grayscale values in (a), (b), and (c) correlate with density, in (d) white color labels the pore and black color the matrix.
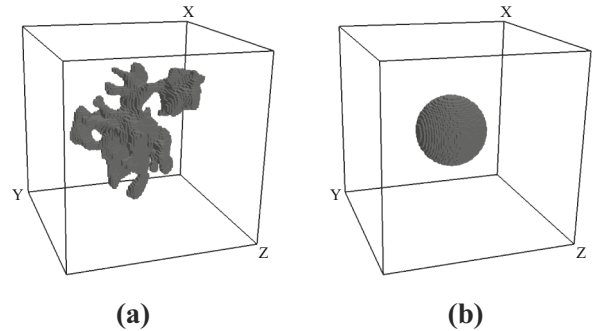

Fig. 2. Geometries of the voids. (a) Realistic pore shape. (b) Idealized pore shape.

of the volume element (Fig. 2b). The shape of this pore resembles convex-shaped gas pores that result from polymer degassing.[14] The ratio of total voxels in this sphere-shaped pore to voxels located at its surface is 0.243, i.e. significantly smaller than in the case of the realistic experimentally measured pore.

Model Parameters

For both, the crystal plasticity as well as the damage model, parameters need to be selected. Although we aim at obtaining qualitative results, where the exact values of the parameters for the constitutive models are of minor interest, their origin is briefly given in the following paragraphs for the sake of completeness.

Table I. Values for the elastic and plastic response of the aluminum matrix

Property	Value	Unit
C_{11}	106.8	GPa
C_{12}	60.4	GPa
C_{44}	28.3	GPa
$\dot{\gamma}_0$	0.001	s^{-1}
τ_0	80.0	MPa
τ_∞	210.0	MPa
h_0	80.0	MPa
a	0.9	
n	20.0	
Coplanar $h_{\alpha\beta}$	1.0	
Non-coplanar $h_{\alpha\beta}$	1.4	

Crystal Plasticity Constitutive Model The parameters used for the crystal plasticity constitutive model are based on an existing dataset that reproduces the behavior of a soft aluminum alloy.[22] Since obtaining suitable parameters for the employed phenomenological model[33,34] or the development of a physics-based model[35–37] are challenging tasks by themselves, the existing parameters (except for the elastic constants[38]) are manually adjusted to increase yield point and hardening. The parameters used are given in Table I and the resulting stress–strain curve (including damage) canbe seen in Fig. 3b.

Isotropic elasto-plastic behavior (without additional damage mechanisms) is assumed inside the pore as it cannot be taken out of the computation domain as in, e.g., finite element simulations. Low elastic stiffness ($C_{11} = 10.0$ MPa, $C_{12} = 6.7$ MPa) and initial and final yield strength of 10.0 MPa and 63.0 MPa, respectively, ensure that the residual mechanical response of the pore does not influence the simulation results.**

Phase Field Fracture Model The damage model is parameterized in terms of the fracture surface energy, g_0, characteristic length scale, l_0, and mobility M. The characteristic length scale l_0 was set to the length of two voxels and the residual stiffness for $\varphi = 0$ was set to 0.01% of the elastic stiffness tensor in the undamaged bulk material. A mobility of $M = 0.01$ is used, which is reasonable for the strain rates used in the present work. The fracture surface energy was adjusted such that the macroscopic stress–strain curve of a polycrystalline material shows the expected behavior of failure at the later stage of the plastic deformation. To this end a simple grain structure of 60 grains with randomly selected orientations created by a standard Voronoi tessellation approach was created. The stress–strain curve for uniaxial loading in x-direction and the corresponding crack surface for the finally selected value of $g_0/l_0 = 5.0\,\text{MN}\,\text{m}^{-1}$ are shown in Fig. 3.

** For $\varepsilon = 0.25$, i.e. a strain 5 times higher than the maximum global strain in any simulation presented here, a maximum stress of $\sigma \leq 3$ MPa for uniaxial loading will be reached.
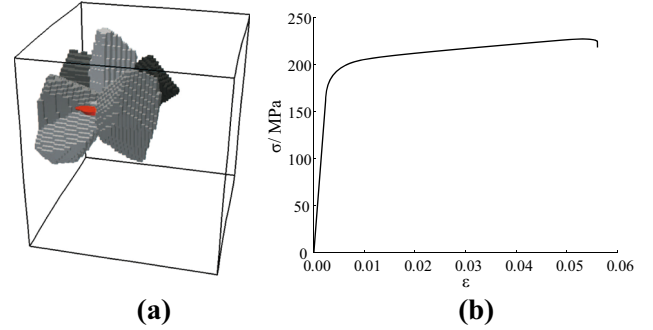

(a)　　　　**(b)**

Fig. 3. Results of the polycrystal simulation for validating the damage parameters. (a) Crack (red, isosurface $\varphi = 0.2$) and surrounding crystallographic grains (grayscale). Loading is along vertical direction. (b) Stress–strain curve showing damage-induced softening before failure (Color figure online).

Loading

Uniaxial tension along x-direction is applied at a rate of 1×10^{-3} s^{-1} with a time step of 0.0025 s. For the cube orientation, this corresponds to loading along the [1 0 0] direction, for the rotated cube orientation to loading along the [1 1 0] direction and for the P orientation along the [1 1 1] direction.

RESULTS

The results obtained for the three simulations of the experimentally obtained pore shape are presented first, followed by the results of the three accompanying simulations on the spherical inclusions.

Simulations Using a Realistic Pore Shape

The stress–strain curves up to a stress drop of 10 MPa[†] for the three different crystallographic orientations assigned to the matrix material are shown in Fig. 4 together with the stress–strain response when the damage model is disabled. It can be seen that the elastic and plastic response strongly depends on the crystallographic orientation: an alignment of the [1 0 0] direction with the loading direction (cube orientation) shows—elastically and plastically—the softest response followed by an alignment of the [1 1 0] direction (rotated cube orientation) with the loading axis and an alignment of [1 1 1] direction with the loading axis (P orientation). In contrast to the response of the polycrystal (Fig. 3b), less softening and a more brittle behavior is observed for all three crystallographic orientations. For the matrix with P orientation, fracture sets in before the elastic–plastic transition starts and the volume elements with matrix orientation of (rotated) cube orientation fail when loaded beyond the yield point.

[†]The further stress–strain response in the unstable crack propagation regime (essentially a vertical line) is not shown as artifacts introduced by the self-interaction of the crack caused by the periodic boundary conditions cannot be excluded.

Coupled Crystal Plasticity–Phase Field Fracture Simulation Study on Damage Evolution
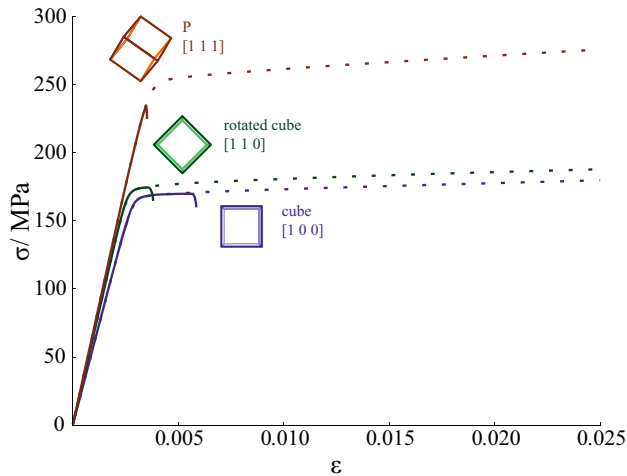Around a Void: Pore Shape Versus Crystallographic Orientation

Fig. 4. Stress–strain curves of the volume element with realistic pore inclusion for the three different crystallographic orientations of the aluminum matrix. Loading is vertical to the sketched unit cells. Dashed lines show the stress strain response without damage.
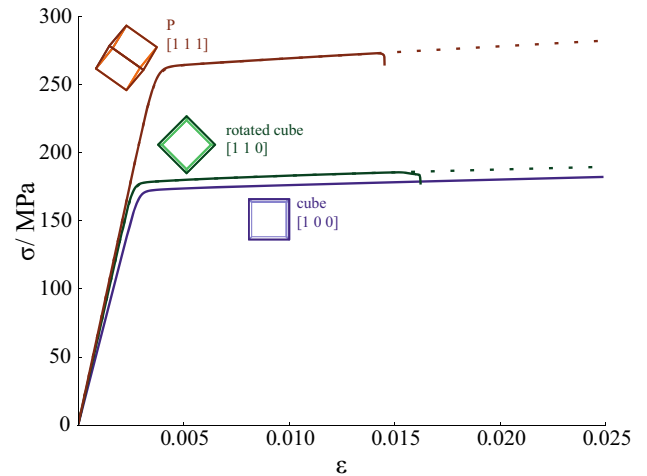

Fig. 6. Stress–strain curves of the volume element with idealized pore inclusion for the three different crystallographic orientations of the aluminum matrix. Loading is vertical to the sketched unit cells. Dashed lines show the stress strain response without damage.
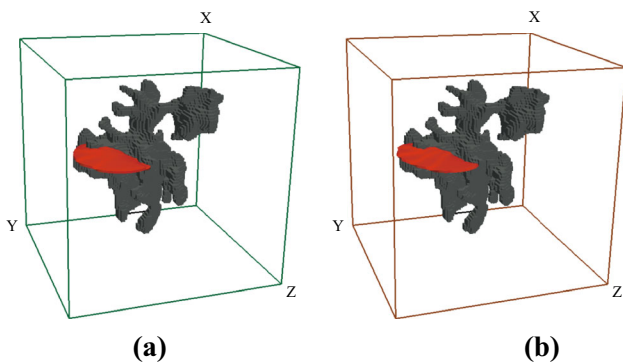

(a)   **(b)**

Fig. 5. Crack surfaces (red, iso-surface $\varphi = 0.2$) around the pore with realistic shape for two crystallographic orientations of the aluminum matrix. Loading is along *x*-direction. (a) Rotated cube orientation. (b) P orientation (Color figure online).
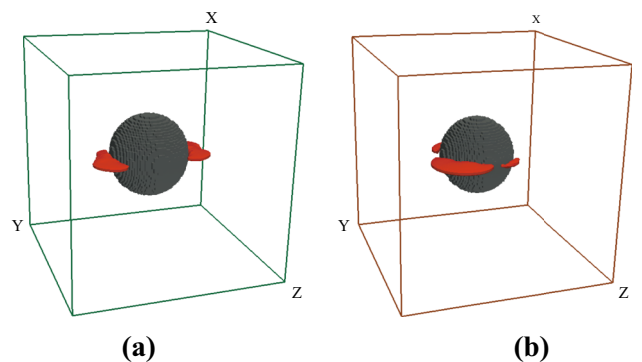

(a)   **(b)**

Fig. 7. Crack surfaces (red, iso-surface $\varphi = 0.3$) around the pore with idealized shape for two crystallographic orientations of the aluminum matrix. Loading is along *x*-direction. (a) Rotated cube orientation. (b) P orientation (Color figure online).

The crack surfaces in the loading regime of unstable crack propagation are shown in Fig. 5 for the cases that the rotated cube and the P crystallographic orientation are assigned to the matrix. It can be seen that the shape of the pore locates the crack initiation in a narrow C-shaped area of the matrix for both crystallographic orientations. No significant effect of the crystallographic orientation on the crack is observed (this holds also for the cube orientation not shown here).

Simulations Using an Idealized Pore Shape

Figure 6 shows the stress–strain curves for the three different crystallographic orientations assigned to the matrix material together with the stress–strain response when the damage model is disabled. In contrast to the simulations using a realistic pore shape, damage sets in at much higher deformation beyond the yield point: for all crystallographic orientations investigated the yield point is passed and the cube orientation suppresses damage entirely within the investigated strain regime ($\varepsilon = 0.05$). Some damage-induced softening is observed for the rotated cube orientation while the P orientation shows a fully brittle behavior after the onset of damage.

The crack surfaces at a strain level close to failure are shown in Fig. 7 for the two simulations in which damage is observed. While for the rotated cube orientation, two equi-sized cracks at opposing sides of the sphere are formed, a larger crack accompanied by two smaller cracks located orthogonally forms in the P orientation. By investigating the damage evolution over time in the P-oriented matrix (not shown here), it can be seen that damage initiates at all three points at the same time but propagates much faster only at one of these positions.

DISCUSSION

Based on the results presented above, a qualitative understanding of the interactions between the shape of a void and the crystallographic orientation can be derived. First of all, the crystallographic orientation of the adjacent matrix material and the shape of the pore both have a strong effect on the strain to fracture. The influence of crystallographic orientation is less pronounced for the realistic inclusion shape as obtained by μ-CT in comparison to the idealized case of a spherical void. The evolving crack surfaces explain this behavior: the pore with realistic shape introduces a stress localization in a narrow region of the matrix surrounded by a C-shaped part of the void and hence determines the location of the crack initiation. The associated stress peaks which lie significantly above the average stress level render the orientation-dependent material behavior in this situation comparatively unimportant. In contrast, the geometrically isotropic and convex shape of the idealized pore does not favor any location such that only the elastic and plastic anisotropy of the matrix material governs the damage evolution. For the matrix with cube orientation, eight slip systems with the same high Schmid factor of 0.41 enable deformation along the prescribed loading direction, and the remaining four systems allow for lateral contraction imposed by the boundary conditions. Therefore, in the case of the spherical inclusion, no damage is observed and, in the case of the measured pore, the highest fracture toughness among the investigated orientations is achieved. Only two slip systems resolve any shear stress along the loading direction (Schmid factor 0.41) in the rotated cube orientation such that plastic deformation is much more costly and damage sets in at the locations in the vicinity of the void. The situation in the P-oriented matrix is again completely different: all slip systems have a non-zero Schmid factor, but their values show a large spread from 0.46 to 0.02 such that an inhomogeneous and high stress state is expected and early damage initiation is promoted.

The presented results clearly reveal that damage in crystalline materials is governed by various coupled—partly competing and partly enhancing—mechanisms and the interactions between them. As an example, the crystallographic orientation determines the primary growing crack around the sphere-shaped void which in turn results in higher stresses on initially slower propagating cracks. Hence, fully coupled damage and crystal plasticity modeling approaches are indeed required to capture the influence of stress re-distribution and slip system activation. For a complex-shaped pore, the absolute levels of stress at failure can depend on crystallographic orientation while the location of crack initiation is fully determined by the shape of the pore.

CONCLUSION AND OUTLOOK

The results presented here enable a qualitative understanding of the fracture around voids embedded in a metal matrix. For obtaining quantitative results under quasi-static loading conditions, a more detailed crystal plasticity model and/or extensive parameter fitting to experimental results would be required. However, additional effects such as the influence of in-grain crystallographic scatter, orientation gradients, or the interaction between multiple inclusions and/or multiple grains, can be easily investigated with the present approach, where it should be noted, however, that the latter would require the use of significantly larger volume elements and, hence, increased computational efforts.

For a strong coupling between experimental and simulated results, determination of the crystallographic orientation is an essential prerequisite. While serial sectioning electron backscatter diffraction techniques allow the characterization of crystallographic orientation including the above-mentioned in-grain orientation scatter,[39] they prohibit subsequent experiments. Synchrotron measurements, in contrast, can determine polycrystalline microstructures at high spatial resolution in a non-destructive manner.[40] As an alternative available at laboratory scales, a diffraction contrast tomography enhancement for the current μ-CT system (known as LabDCT[41]) enables non-destructive characterization of individual grains, however at the cost of having only grain average orientation information.

Even though damage is often modeled assuming an isotropic constitutive behavior, not only elastic and plastic properties of crystals depend on their orientation but also the damage mechanism itself. The use of cleavage plane-based formulations for anisotropic brittle fracture[10] would enable the investigation of such effects. Alternatively, if ductile damage—governed by void formation and coalescence—is experimentally observed, these phenomena should be directly modeled to replace the brittle damage model employed here.

Finally, it should be noted that failure under quasi-static loading is not the situation typically observed for the matrix material investigated here. As it is known that, for cyclic loading cases, dislocation-mediated void formation phenomena at the microstructural level are of importance, and can totally reverse trends observed for quasi-static loading (i.e. a spherical inclusion is more detrimental than a sharp notch), physics-based models for these processes that take crystallographic orientation into account are required.

OPEN ACCESS

REFERENCES

1. F. Roters, P. Eisenlohr, L. Hantcherli, D.D. Tjahjanto, T.R. Bieler, and D. Raabe. *Acta Mater.* 58, 1152 (2010).
2. G.Z. Voyiadjis. *Handbook of Damage Mechanics* (New York: Springer, 2015).
3. G.Z. Voyiadjis and N. Mozaffari. *Int. J. Solids Struct.* 50, 3136 (2013).
4. N. Mozaffari and G.Z. Voyiadjis. *Phys. D* 308, 11 (2015).
5. N. Mozaffari and G.Z. Voyiadjis. *Int J Plast.* 83, 55 (2016).
6. C. Miehe, F. Welschinger, and M. Hofacker. *Int. J. Numer. Meth. Eng.* 83, 1273 (2010).
7. C. Kuhn and R. Müller. *Eng. Frac. Mech.* 77, 3625 (2010).
8. R. Spatschek, E. Brener, and A. Karma. *Philos. Mag.* 91, 75 (2011).
9. P. Shanthraj, L. Sharma, B. Svendsen, F. Roters, and D. Raabe. *Comput. Methods Appl. Mech.* 312, 167 (2016).
10. P. Shanthraj, B. Svendsen, L. Sharma, F. Roters, and D. Raabe. *J. Mech. Phys. Solids* 99, 19 (2017).
11. B. Skallerud, T. Iveland, and G. Härkegård. *Eng. Fract. Mech.* 44, 857 (1993).
12. Y.X. Gao, J.Z. Yi, P.D. Lee, and T.C. Lindley. *Fatigue Fract. Eng. Mech.* 27, 559 (2004).
13. M. Wicke, M. Luetje, I. Bacaicoa, and A. Brueckner-Foit. *Proc. Struct. Integr.* 2, 2643 (2016).
14. S. Dezecot, V. Maurel, J.-Y. Buffiere, F. Szmytka, and A. Koster. *Acta Mater.* 123, 24 (2017).
15. F. Roters, P. Eisenlohr, C. Kords, D.D. Tjahjanto, M. Diehl, and D. Raabe, in O. Cazacu, editor *Proc. IUTAM*, 3, 3 (Elsevier, Amsterdam, 2012).
16. J.W. Hutchinson. *Proc. R. Soc. Lond. A Math.* 348, 101 (1976).
17. D. Peirce, R.J. Asaro, and A. Needleman. *Acta Metall.* 30, 1087 (1982).
18. B. Bourdin, G.A. Francfort, and J.-J. Marigo. *J. Mech. Phys. Solids* 48, 797 (2000).
19. K. Pham, H. Amor, J.-J. Marigo, and C. Maurini. *Int. J. Damage Mech.* 20, 618 (2011).
20. B. Bourdin, C.J. Larsen, and C.L. Richardson. *Int. J. Fract.* 168, 133 (2011).
21. C. Miehe, F. Aldakheel, and A. Raina. *Int. J. Plast.* 84, 1 (2016).
22. P. Eisenlohr, M. Diehl, R.A. Lebensohn, and F. Roters. *Int. J. Plast.* 46, 37 (2013).
23. P. Shanthraj, P. Eisenlohr, M. Diehl, and F. Roters. *Int. J. Plast.* 66, 31 (2015).
24. H. Moulinec and P. Suquet. *Comput. Methods Appl. Mech.* 157, 69 (1998).
25. S.-B. Lee, R.A. Lebensohn, and A.D. Rollett. *Int. J. Plast.* 27, 707 (2011).
26. J. Sliseris, H. Andrä, M. Kabel, B. Dix, B. Plinke, O. Wirjadi, and G. Frolovs. *Mech. Mater.* 79, 73 (2014).
27. J. Zeman, J. Vondřejc, J. Novák, and I. Marek. *J. Comput. Phys.* 229, 8065 (2010).
28. L. Gélébart and R. Mondon-Cancel. *Comput. Mater. Sci.* 77, 430 (2013).
29. J. Zeman, T.W.J. De Geus, J. Vondřejc, R.H.J. Peerlings, and M.G.D. Geers, *Int. J. Numer. Methods Eng.* (2017).
30. T.W.J. De Geus, J. Vondřejc, J. Zeman, R.H.J. Peerlings, and M.G.D. Geers, *Comput. Methods Appl. Mech.* 318, 412 (2017).
31. S. Van Der Walt, J.L. Schönberger, J. Nunez-Iglesias, F. Boulogne, J.D. Warner, N. Yager, E. Gouillart, and T. Yu. *PeerJ* 2, e453 (2014).
32. L. Grady. *IEEE Trans. Pattern Anal. Mach. Intell.* 28, 1768 (2006).
33. C. Zambaldi, Y. Yang, T.R. Bieler, and D. Raabe. *J. Mater. Res.* 27, 356 (2012).
34. C.C. Tasan, M. Diehl, D. Yan, C. Zambaldi, P. Shanthraj, F. Roters, and D. Raabe. *Acta Mater.* 81, 386 (2014).
35. A. Alankar, I.N. Mastorakos, and D.P. Field. *Acta Mater.* 59, 5936 (2009).
36. S.L. Wong, M. Madivala, U. Prahl, F. Roters, and D. Raabe. *Acta Mater.* 118, 140 (2016).
37. D. Cereceda, M. Diehl, F. Roters, D. Raabe, J.M. Perlado, and J. Marian. *Int. J. Plast.* 78, 242 (2016).
38. J.F. Thomas. *Phys. Rev.* 175, 955 (1968).
39. A. Khorashadizadeh, D. Raabe, S. Zaefferer, G.S. Rohrer, A.D. Rollett, and M. Winning. *Adv. Eng. Mater.* 13, 237 (2011).
40. R. Pokharel, J. Lind, S.F. Li, P. Kenesei, R.A. Lebensohn, R.M. Suter, and A.D. Rollett. *Int. J. Plast.* 67, 217 (2015).
41. S.A. McDonald, P. Reischig, C. Holzner, E.M. Lauridsen, P.J. Withers, A.P. Merkle, and M. Feser. *Sci. Rep.* 5, 14665 (2015).